

EVOLUTION OF THE STELLAR MASS-GAS-PHASE METALLICITY  
RELATION OVER SEVEN GIGAYEARS

By

CAROLINE ELIZABETH MCCORMICK

---

A Thesis Submitted to The Honors College  
In Partial Fulfillment of the Bachelors degree  
With Honors in  
Astronomy

THE UNIVERSITY OF ARIZONA

MAY 2021

Approved by:

---

Dr. Chun Ly

# Evolution of the Stellar Mass–Gas-Phase Metallicity Relation over Seven Gigayears

Caroline McCormick

## Abstract

Galaxy evolution can be understood by measuring characteristic properties of the diffuse, ionized gas within galaxies. The gas-phase metallicity ( $Z$ ), or the chemical content, is one measurement that can tell us about the cumulative star formation in a galaxy while taking into account galactic gas flows. In my Honors thesis, I analyzed  $\sim 4,000$  galaxy spectra at redshift ( $z$ )  $\approx 1$  from the DEEP2 Galaxy Redshift Survey to derive metallicities for galaxies. Unlike previous studies, my analyses utilized the electron temperature ( $T_e$ ) method to determine more robust measurements of gas temperature and metallicity. The  $T_e$  method uses the [O III] $\lambda 4363$  emission line as a direct  $T_e$  probe. However, because of its weak signal, I used a stacking approach to combine the spectra of hundreds of individual galaxies of similar stellar masses ( $M_*$ ) to increase the detection of [O III] $\lambda 4363$ . I constructed six robust stellar mass composites: four with [O III] $\lambda 4363$  detections and two with robust non-detections of [O III] $\lambda 4363$ . With derived average metallicities for different stellar mass composite spectra, I then constructed a  $M_*$ – $Z$  relation that is  $\sim 0.1$  dex lower in metallicity at a given stellar mass than the relation for local galaxies (Andrews & Martini 2013). This result indicates that chemical enrichment in galaxies has increased by  $\sim 0.1$  dex in the past seven gigayears of evolution.

## 1 INTRODUCTION

Astronomers seek to understand galaxy evolution by studying three main physical processes that occur in galaxies: gas accretion, star formation, and gas loss due to dying stars (e.g., Tremonti et al. 2004). Taking measurements of the physical properties that characterize the interstellar gas and understanding the physics behind these properties allows us to understand these galactic processes.

An important physical property of galaxies is the gas-phase abundance of heavy elements,<sup>1</sup> or “metallicity” ( $Z$ ). Metallicity provides insights on the stars within galaxies, while taking into account the flow of gaseous material into and out of a galaxy. During a star’s lifetime, it will fuse heavy elements within its interior until it becomes unstable. Massive stars are of great interest as they produce a high proportion of heavy metals, and instabilities toward the end of their lives lead to a violent explosion, causing large outflows of material into the interstellar medium. Because massive stars play a tremendous role in changing the metal content in a galaxy, one of their most common by-products, oxygen gas, is used as a proxy to determine metallicity.

It is thought that an inherent relationship ex-

ists between metallicity and total stellar mass<sup>2</sup> ( $M_*$ ) since metals are formed from massive stars. Such a relationship has been found for local galaxies, or galaxies at low redshift<sup>3</sup> ( $z \lesssim 0.2$ ; e.g., Tremonti et al. 2004; Andrews & Martini 2013), but a relation for galaxies at higher redshift ( $z \gtrsim 0.2$ ) has been poorly determined. Until recently, galaxy evolution studies have assumed that high-redshift galaxies have analogous interstellar gas properties as those in the local universe. However, studies have shown that *indirect* diagnostic optical emission line ratios used to determine metallicities vary across cosmic time (e.g., Kewley et al. 2013). Therefore, more direct techniques are needed to accurately understand the interstellar gas properties at high redshifts. With more direct measurements of metallicity, a  $M_*$ – $Z$  relation for high-redshift galaxies can be studied to understand the degree of chemical enrichment evolution.

A more direct technique of determining metallicities is called the electron temperature ( $T_e$ ) method, which utilizes the inverse correlation between the abundance of metals in a gas and the gas temperature. The presence of metals in diffuse gas is connected to the temperature because metals are efficient at absorbing and re-emitting collisional energy from free electrons, thus lowering the gas tem-

<sup>1</sup>In astronomy, “heavy elements” are all elements heavier than helium.

<sup>2</sup>The combined mass from all of the stars in a galaxy.

<sup>3</sup>Redshift is denoted by a lowercase  $z$ .

perature. Specifically, this kinetic energy transferred to metal ions causes bound electrons to be excited. After some time, these excited electrons will spontaneously release their energy as photons (i.e. the electrons de-excite by moving to a lower energy level). This results in an emission line where the energy escapes and effectively cools the gas.

To measure  $T_e$ , the relative strength of the [O III] $\lambda$ 4363 emission line compared to the [O III] $\lambda$ 5007 emission line is often used (Aller 1984; Osterbrock 1989). The [O III] $\lambda$ 4363 emission line represents the transition of a bound electron in doubly ionized oxygen atoms ( $O^{++}$ ) from a relatively high energy level to a lower energy level (see Figure 1). A large transfer of energy is needed to excite bound electrons in  $O^{++}$  to this high energy level.

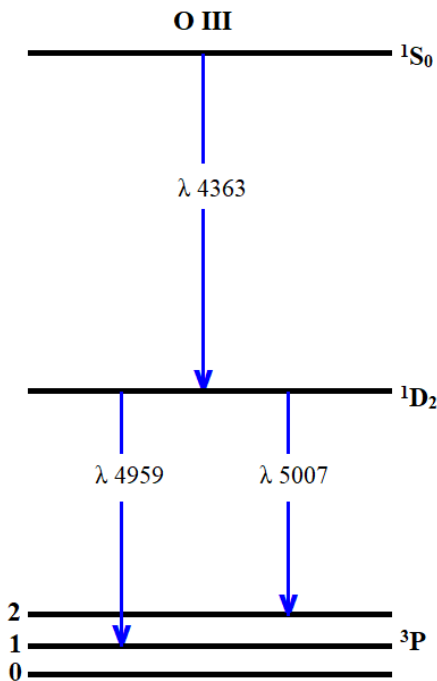


Figure 1: Energy diagram for  $O^{++}$  showing the transitions utilized in determining  $T_e$ : [O III] $\lambda$ 4363, [O III] $\lambda$ 4959, and [O III] $\lambda$ 5007. Energy transition increases upward.

Utilizing [O III] $\lambda$ 4363 measurements via the  $T_e$  method is one of the most reliable methods of determining metallicities. However, this technique is often daunting due to [O III] $\lambda$ 4363 being an inherently weak emission line, especially in metal-rich galaxies. Obtaining a reliable flux measurement of [O III] $\lambda$ 4363 in a single galaxy can be nearly impossible, as it is often hidden in the noise. Also, since metal-poor galaxies have stronger [O III] $\lambda$ 4363 lines than metal-rich galaxies, utilizing single-galaxy measurements

will lead to a biased  $M_*$ - $Z$  relation.

To overcome these problems, my thesis project implements a spectral stacking technique, previously explored by Andrews & Martini (2013) for local galaxies, to yield average detections of the weak [O III] $\lambda$ 4363 emission line and thus average electron temperature and gas metallicity estimates at higher redshifts. To accomplish this, I use spectra from the DEEP2 Galaxy Redshift Survey (Newman et al. 2013), which surveyed thousands of  $z \sim 1$  galaxies.

In this project, I use emission-line fluxes from oxygen and hydrogen optical lines to determine gas properties of high-redshift galaxies, such as metallicity. In doing so, I also quantify how metallicity relates to the stellar mass of galaxies over seven gigayears. The outline of my thesis is as follows. Section 2 describes the spectroscopic data survey used for this study and photometric data for stellar mass estimates. Section 3 outlines the methodology for spectral stacking, how emission lines are fit, and measurement error analysis. Section 4 explains my analysis of the spectroscopic data and how I obtained dust correction factors,  $T_e$ , and metallicities. Finally in Section 5, the current results are presented, and the significance of the findings in galactic evolution studies is discussed in Section 6.

## 2 DATA

### 2.1 SPECTROSCOPIC DATA

The spectroscopic data utilized in this study are from the DEEP2 Galaxy Redshift Survey, which is the largest redshift survey of galaxies at  $z \sim 1$  to date (Newman et al. 2013). The goal of this survey is to obtain redshifts for several thousand galaxies. The DEEP2 Survey was conducted using the Keck II 10-m telescope in Hawaii, and the spectra were obtained using the high resolution ( $R \sim 6000$ ) DEIMOS (DEep Imaging Multi-Object Spectrograph; Faber et al. 2003) spectrograph. Spectra for  $\approx 50,000$  galaxies were obtained with spectral coverage between 6500Å and 9100Å.

Of these 50,000 galaxies, reliable redshifts using two or more emission lines were found for  $\sim 38,000$  at  $z > 0.7$ . The sample was further limited in Ly et al. (2015) by requiring that rest frame spectra include the range 3720–5010Å so that optical hydrogen and oxygen emission lines may be used to determine temperature and metallicity. This criterion gave a total of 4,140 spectra. From the 4,140 spectra, I identified six spectra that indicated the existence of systematic errors in the flux calibration. Specifically, they had

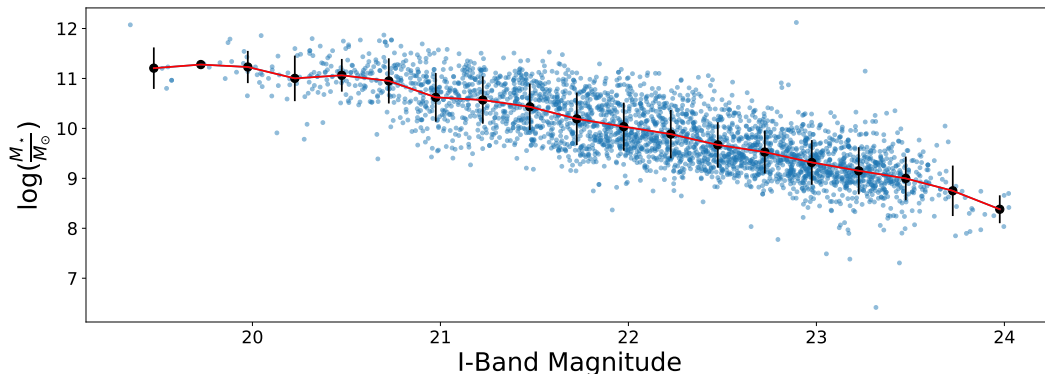


Figure 2: Stellar mass as a function of  $I$ -band photometry. The blue points are  $\sim 3,000$  galaxies with robust stellar masses. The black points and red line show a linear interpolation that was used to map  $I$ -band photometry to stellar masses when not enough wavebands were available for stellar mass estimates.

significantly higher deviations as compared to other spectra taken in similar observing conditions. Thus, these spectra were excluded, yielding a working spectroscopy sample of 4,134 spectra.

## 2.2 PHOTOMETRIC DATA AND STELLAR MASS

The photometric data for the DEEP2 Survey used in this project were obtained from multiple telescopes and instruments. It consists of  $BRI$  photometry from the Canada-France-Hawaii Telescope (CFHT) and  $ugriz$  photometry from the Sloan Digital Sky Survey and CFHT Legacy Survey. These photometric datasets were compiled as extended photometric catalogs for DEEP2 by [Matthews et al. \(2013\)](#).

To derive stellar masses, a former team member constructed the spectral energy distribution (SED) of all DEEP2 galaxies from available photometric data and then compared and fitted them against model SEDs for galaxies. To conduct the SED fitting, the Python Implementation of Code Investigating GALaxy Emission (CIGALE; [Boquien et al. 2019](#)) was used. The star formation history (SFH) models are those of [Bruzual & Charlot \(2003\)](#) and consist of (1) delayed exponential (“sfhdelayed”) with different  $e$ -folding times of 0.1, 0.25, 0.5, 1, 2, 4, 6, and 8 Gyr; (2) an adopted [Chabrier \(2003\)](#) initial mass function (IMF); (3) solar metallicity ( $Z = 0.02$ ); and (4) dust attenuation using a power-law relation  $A \propto \lambda^{-0.7}$ ,  $A_V$  between 0.0 and 3.0 mag (0.5 mag increments), a scaling factor between young and old population of 0.44 ([Calzetti et al., 2000](#)), and a 2175Å bump with variable amplitude (0.0, 0.5, or 1.0). An illustration of the derived stellar mass against the  $I$ -band pho-

tometry is displayed in [Figure 2](#).

For some ( $\sim 25\%$ ) of the galaxies, stellar masses were not available. This problem stems from limited photometric bands. For example, some galaxies only had  $BRI$  photometry data from the CFHT, which is insufficient for estimating stellar masses. To maximize the sample, I utilized the  $I$ -band photometry provided by DEEP2 for  $\sim 3,000$  galaxies to interpolate stellar mass values for those galaxies without stellar masses ([Figure 2](#)). After substituting interpolated values for galaxies without reliable stellar masses, I excluded any galaxies from the sample with a stellar mass above  $10^{13} M_\odot$  ( $\sim 40$  galaxies). The final sample after all of these criteria were met consists of 4,087 galaxies.

## 3 METHODOLOGY

An individual high-redshift galaxy has an  $[\text{O III}]\lambda 4363$  emission line that is almost undetectable, which makes it difficult to determine metallicities for large samples of individual galaxies. To improve signal detection, I instead implemented a spectral stacking technique that combines the spectral signal from multiple galaxies ([Andrews & Martini 2013](#)). This approach allows for more robust measurements by reducing the instrumental and background noises, yielding average fluxes of  $[\text{O III}]\lambda 4363$  and other emission lines. The strength of  $[\text{O III}]\lambda 4363$  will vary with the physical properties of galaxies, such as stellar mass. Therefore, to yield representative averages, I stack spectra based on a primary property of galaxies, stellar mass.

Table 1: Adaptive Stellar Mass Binning Combinations

Trial (1)	$N_{\text{gal}}$ (2)	Bins (3)	$N_{\text{D}}$ (4)	$N_{\text{RND}}$ (5)	$N_{\text{ND}}$ (6)
1	400, 400, 400, 800, 1044, 1043	6	2	2	2
2	300, 300, 600, 1444, 1443	5	3	1	1
3	150, 150, 300, 600, 1444, 1443	6	4	1	1
4	75, 75, 75, 75, 300, 600, 1444, 1443	8	4	3	1
5	75, 112, 113, 300, 600, 1444, 1443	7	4	2	1

(1) Adaptive binning trial number. (2) Number of galaxies in each bin (increasing in stellar mass). (3) Number of stellar mass bins. (4) Number of bins (composite spectra) with [O III] $\lambda$ 4363 detections ( $S/N \geq 3$ ). (5) Number of composite spectra with robust non-detections of [O III] $\lambda$ 4363 ( $S/N < 3$ , [O III] $\lambda$ 5007  $S/N \geq 100$ ). (6) Number of composite spectra with non-detections of [O III] $\lambda$ 4363 ( $S/N < 3$ , [O III] $\lambda$ 5007  $S/N < 100$ ).

Table 2: Summary of Stellar Mass Bins for Trial #5

Bin ID (1)	$N_{\text{gal}}$ (2)	Detection (3)	$\log(M_{\star}/M_{\odot})$		
			min (4)	max (5)	avg (6)
1	75	D	6.415	8.584	8.236
2	112	D	8.584	8.800	8.707
3	113	D	8.800	8.913	8.862
4	300	R	8.913	9.079	9.003
5	600	D	9.079	9.347	9.212
6	1444	R	9.347	10.021	9.669
7	1443	N	10.021	12.121	10.601

(1) Stellar mass bin ID. (2) Number of galaxies in each stellar mass bin. (3) [O III] $\lambda$ 4363 detection where D=“Detection,” R=“Reliable non-detection,” and N=“Non-detection.” (4) Stellar mass of the least massive galaxy in each bin. (5) Stellar mass of the most massive galaxy in each bin. (6) Average stellar mass of each bin.

### 3.1 BINNING IN STELLAR MASS

I investigated the reliability of [O III] $\lambda$ 4363 detections as a function of stellar mass by grouping galaxies with two approaches: (1) equally-sized “bins” and (2) bins with a varying number of galaxies. First, with the approach of equal-sized stellar mass bins, I experimented with five predefined bin sizes of 200, 300, 400, 600, and 800 galaxies, which resulted in 16<sup>4</sup>, 13, 10, 6, and 5 bins, respectively. Ideally, the average spectrum from each bin should result in a detectable signal of [O III] $\lambda$ 4363. However, I found that using the equal-sized bin method resulted in low-mass bins displaying a strong [O III] $\lambda$ 4363 detection and more massive bins lacking a detection. With this approach, I would only be able to derive temperatures and metal-

licities from a small number of bins, and the results would be biased toward low-mass galaxies. Therefore to maximize the number of stellar mass bins with detections and to study a larger mass range of galaxies, I adopted an adaptive binning technique, which was my second approach.

The adaptive binning technique accounts for the varying strength of [O III] $\lambda$ 4363 with stellar mass by performing finer sampling for galaxies with expected high [O III] $\lambda$ 4363 strengths and shallower sampling in cases with low strengths. For galaxies with low stellar masses, the correlation with lower metallicities would result in a higher [O III] $\lambda$ 4363 strength, thus requiring fewer galaxies in each bin. I experimented with different sets of bin sizes (see Table 1 for the various combinations tried), but I found

<sup>4</sup>The total sample used here was  $\sim 3,000$  galaxies (i.e. these bins did not include the galaxies with interpolated mass).

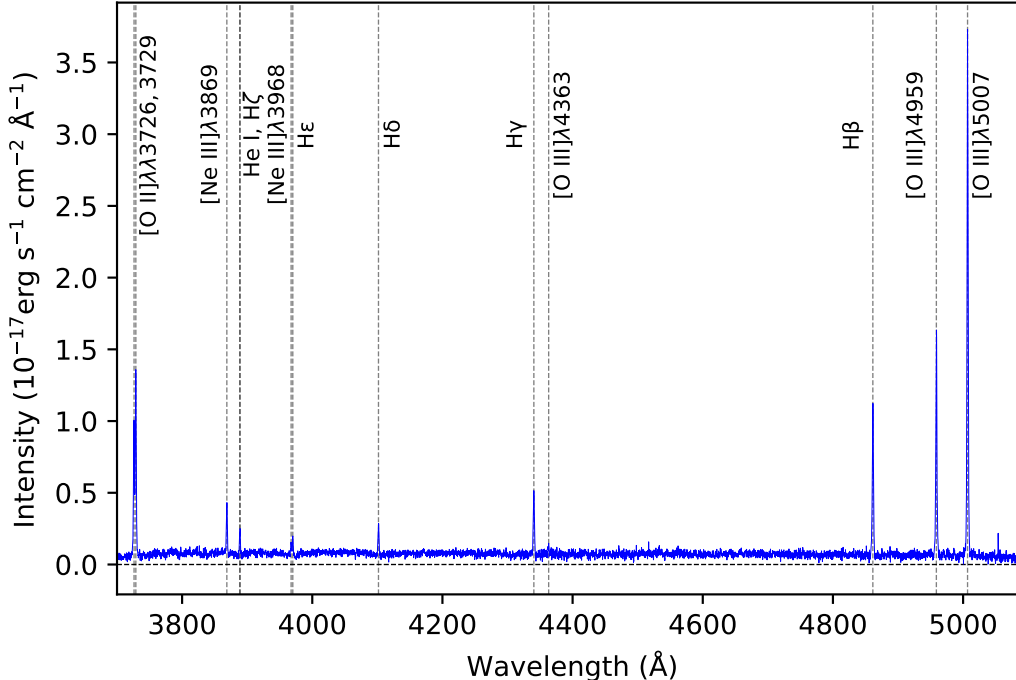


Figure 3: Composite optical spectrum for the lowest stellar mass bin containing 75 galaxies. Vertical dashed lines illustrate locations of emission lines.

that Trial #5 (see Table 1) gave the highest number of stellar mass bins with [O III]λ4363 detections.<sup>5</sup> Of the seven mass bins, four bins produced reliable detections of [O III]λ4363 with signal-to-noise (S/N)  $\geq 3$ . In addition, two of the three remaining bins had robust non-detections as the [O III]λ5007 emission line was detected at  $S/N \gtrsim 100$ , thus providing strong lower limit constraints on gas metallicity. See Table 2 for a summary of the stellar mass bins from Trial #5.

### 3.2 SPECTRAL STACKING

Once the spectra were grouped into bins based on stellar mass, I implemented a spectral stacking technique that averaged out the spectra in each bin to produce a composite spectrum that has reduced noise, thus improving the S/N of [O III]λ4363 (see Figure 3). For reference, Figure 4 illustrates each bin’s composite spectrum zoomed in around [O III]λ4363 and Hγ to show how weak [O III]λ4363 is even with spectral stacking.

An enhancement that was made to improve the spectral stacks was to mask out contamination from the night sky, which consists of OH emission lines produced in Earth’s atmosphere. To correct for this, I

used a list of night skylines and masked around these night skylines prior to stacking.

### 3.3 EMISSION LINE FITTING

Utilizing the stacked spectra, the next step was to measure the flux of each nebular emission line. I was specifically interested in seven emission lines that estimate  $T_e$ , metallicity, and dust contamination: [O II]λ3727, Hδ, Hγ, [O III]λ4363, Hβ, [O III]λ4959, and [O III]λ5007. To measure the flux from each of these emission lines, I used emission-line models to fit the observed lines as closely as possible. The type of model depended on the nature of each of the aforementioned emission lines (see Figure 5)—i.e. whether the profile is a single emission, emission and absorption (e.g., Balmer lines), or double emission. I combined initial guesses of the parameters of the model line with a Python library called `scipy.optimize.curve_fit` to generate these model curves, matching them to the observed emission lines.

First, single lines like [O III]λ4363, [O III]λ4959, and [O III]λ5007 were fitted with a single Gaussian profile. Initial values such as the maximum amplitude, continuum level, central wavelengths, and line widths were provided to the `curve_fit` program.

<sup>5</sup>Trial #4 was not chosen because the distribution of galaxies for the four lowest-mass bins caused relatively high [O III]λ4363 detections in some bins while others were barely detectable.

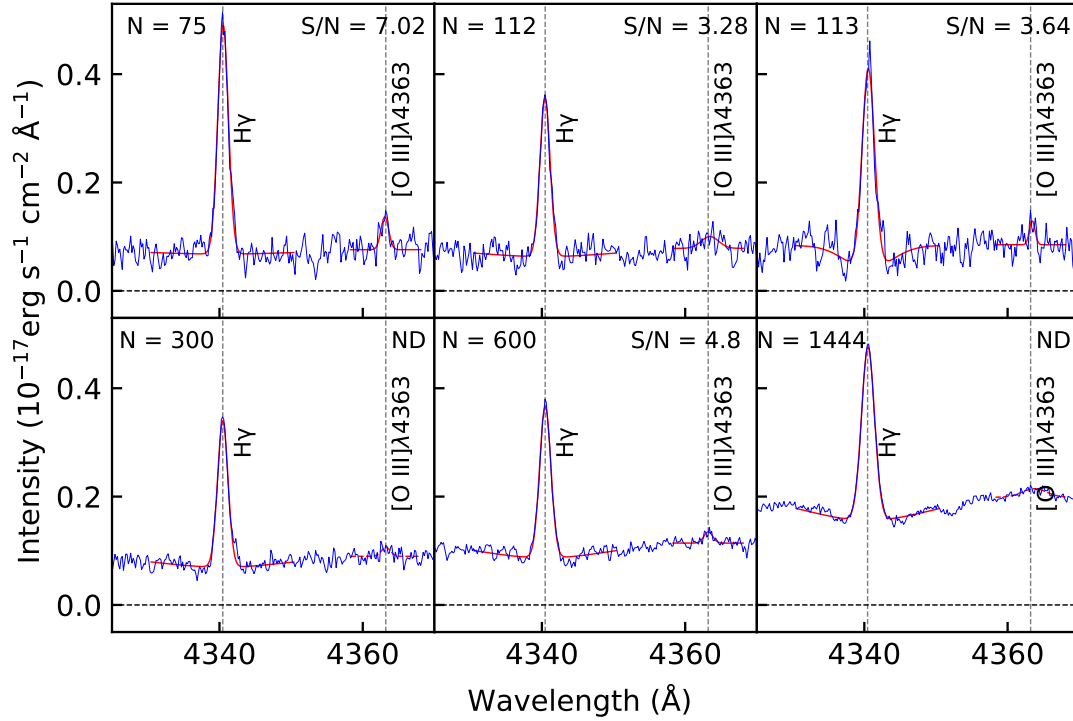


Figure 4: Illustration of  $[\text{O III}]\lambda 4363$  and  $\text{H}\gamma$  measurements from composite spectra for different stellar mass bins. The bins here increase in stellar mass from left to right and top to bottom.  $N$  is the number of galaxies in each bin. The fitting results for  $\text{H}\gamma$  and  $[\text{O III}]\lambda 4363$  are overlaid in red.

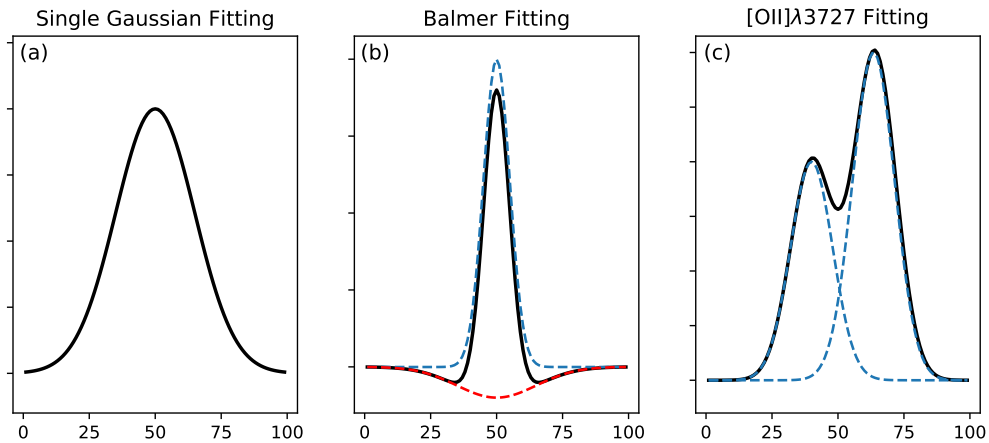


Figure 5: Three Gaussian models used to fit emission lines: (a) single emission (e.g.,  $[\text{O III}]\lambda 4363$ ,  $[\text{O III}]\lambda 4959$ ,  $[\text{O III}]\lambda 5007$ ); (b) emission (blue) and absorption (red) curves (e.g., Balmer lines:  $\text{H}\delta$ ,  $\text{H}\gamma$ , and  $\text{H}\beta$ ); and (c) double-peak emission (e.g.,  $[\text{O II}]\lambda 3727$ ). The black solid lines represent the resultant emission-line fit for each model. Image adapted from [Leimbach \(2020\)](#).

Second, the Balmer lines, such as  $\text{H}\delta$ ,  $\text{H}\gamma$ , and  $\text{H}\beta$ , exhibit emission (from  $\text{H II}$  regions) and absorp-

tion (from stars) features. Therefore to obtain an accurate measurement of the net emission line flux,

I combined two Gaussian profiles: one positive and one negative.

Finally, fitting [O II] $\lambda$ 3727 proved to be more complicated, as it is a blend of two emission lines at 3726Å and 3729Å. Here, I fitted both emission lines simultaneously with a double Gaussian profile that had differing amplitudes and line widths, a fixed wavelength ratio between the two lines, and the same continuum. Then I combined the fluxes from both lines to obtain the strength at 3727Å.

### 3.4 ERROR ANALYSIS

I quantified the extent of uncertainties in my measurements and all derived properties by first randomizing the fluxes of each emission line based on uncertainties from the spectrum. This randomization produced distributions of plausible values for each quantity. Using these distributions of randomized values, I computed derived properties, as discussed in Section 4. Error propagation was only done for stellar mass bins with [O III] $\lambda$ 4363 detections.<sup>6</sup>

## 4 DERIVED PROPERTIES

With emission-line fluxes, I was able to derive critical properties of the interstellar gas such as electron temperature and gas metallicity. In addition, the hydrogen Balmer lines (H $\delta$ , H $\gamma$ , H $\beta$ ) provided an estimate of how dust attenuates light.

<sup>6</sup>Composite spectra that consist of non-detections are excluded from my analyses.

### 4.1 DUST ATTENUATION

To obtain accurate estimates of temperature and gas metallicity, I corrected the emission-line fluxes for dust attenuation. Dust attenuation is the combined effect of absorption and re-emission of photons due to their interaction with dust grains. It alters how much light is observed. In addition, dust attenuates blue light to a greater extent than red light. This effect is due to dust being very efficient at absorbing and re-emitting light with wavelengths comparable to the size of dust grains ( $\approx 0.1\text{--}0.3 \mu\text{m}$ ). The effect of this dust attenuation is that observed flux ratios, e.g., [O II] $\lambda$ 3727/[O III] $\lambda$ 5007, will be lower than their intrinsic values.

To estimate the amount of attenuation, I computed the color excess,  $E(B-V)$ , which quantifies the relative amount of attenuation between two bands/wavelengths,  $B$  and  $V$ . It is used to normalize attenuation at other wavelengths.  $E(B-V)$  can be estimated by comparing the observed ratios of H $\gamma$ /H $\beta$  and H $\delta$ /H $\beta$  to their intrinsic values (Osterbrock 1989):

$$\frac{(\text{H}n/\text{H}\beta)_{\text{obs}}}{(\text{H}n/\text{H}\beta)_0} = 10^{-0.4E(B-V)[k(\text{H}n)-k(\text{H}\beta)]}, \quad (1)$$

where  $k(\lambda) \equiv A(\lambda)/E(B-V)$  and  $A(\lambda)$  is the amount of attenuation at wavelength,  $\lambda$ . Any deviation from the intrinsic flux ratios,  $(\text{H}n/\text{H}\beta)_0$ , will quantify how much reddening has occurred due to dust. To obtain intrinsic flux ratio values, I assumed that Case B recombination occurs in the optically thick H II regions. This assumption provided intrinsic hydrogen flux ratios of  $(\text{H}\gamma/\text{H}\beta)_0 = 0.468$  and  $(\text{H}\delta/\text{H}\beta)_0 = 0.259$ . For

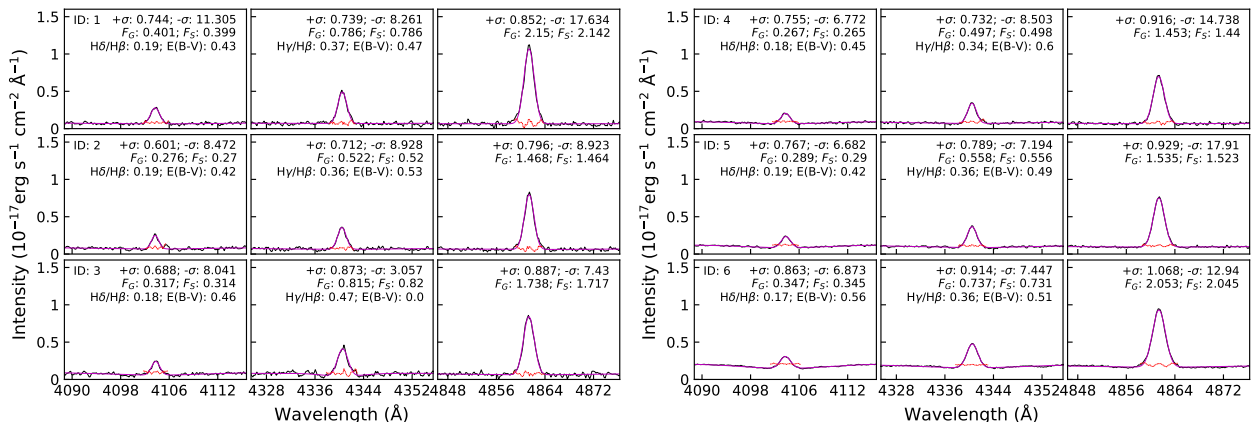


Figure 6: Emission-line fits (magenta) and residuals (red) for Balmer lines used to compute dust attenuation corrections. Each row contains composite spectra (black) for each stellar mass bin; from left to right, the emission lines are H $\delta$ , H $\gamma$ , and H $\beta$ .

Table 3: Summary of Dust Attenuation Analysis

Bin ID	H $\gamma$ /H $\beta$	H $\delta$ /H $\beta$	$E(B-V)$ [H $\gamma$ /H $\beta$ ]	$E(B-V)$ [H $\delta$ /H $\beta$ ]
(1)	(2)	(3)	(4)	(5)
1	0.365 $^{+0.007}_{-0.007}$	0.187 $^{+0.005}_{-0.005}$	0.475 $^{+0.037}_{-0.035}$	0.428 $^{+0.038}_{-0.035}$
2	0.355 $^{+0.009}_{-0.008}$	0.188 $^{+0.007}_{-0.007}$	0.528 $^{+0.046}_{-0.046}$	0.423 $^{+0.050}_{-0.048}$
3	0.469 $^{+0.011}_{-0.011}$	0.182 $^{+0.007}_{-0.007}$	0 $^{+0.046}_{-0.046}$	0.459 $^{+0.054}_{-0.052}$
4	0.342	0.184	–	–
5	0.364 $^{+0.005}_{-0.006}$	0.188 $^{+0.004}_{-0.005}$	0.484 $^{+0.031}_{-0.026}$	0.418 $^{+0.033}_{-0.030}$
6	0.359	0.169	–	–

(1) Stellar mass bin ID. (2)–(3) Observed flux ratio of H $\gamma$  to H $\beta$ , H $\delta$  to H $\beta$ . (4)–(5) Computed  $E(B-V)$  (in units of magnitudes) using H $\gamma$ /H $\beta$ , H $\delta$ /H $\beta$ . Errors and  $E(B-V)$  values were only computed for bins with detections.

$k(\lambda)$ , I adopted Cardelli et al. (1989) attenuation relation, where  $k(\text{H}\beta) = 3.61$ ,  $k(\text{H}\gamma) = 4.17$ , and  $k(\text{H}\delta) = 4.44$ .

The observed H $\gamma$ /H $\beta$  and H $\delta$ /H $\beta$  values were computed by taking the ratio of the flux of each emission line. Figure 6 illustrates the fitting results for each Balmer line and Table 3 provides the observed ratios and computed  $E(B-V)$  values for each composite spectrum.

## 4.2 TEMPERATURE AND METALLICITY

Once the emission-line flux ratios were corrected for dust attenuation, I derived electron temperatures of the interstellar gas and the metallicity of the gas (Izotov et al. 2006; Nicholls et al. 2013). The electron temperature of the gas can be determined from the relative strength of bound electron transitions (e.g., [O III] $\lambda$ 4363, [O III] $\lambda$ 4959, and [O III] $\lambda$ 5007) since free electrons collisionally excite bound electrons of O $^{++}$  in H II regions. The flux ratio of O $^{++}$  emission lines,  $R$ , is defined as:

$$R \equiv \frac{F([\text{O III}]\lambda 4363)}{F([\text{O III}]\lambda \lambda 4959, 5007)}. \quad (2)$$

Here I adopted [O III] $\lambda$ 5007/[O III] $\lambda$ 4959 = 3.1 (Storey & Zeippen 2000) rather than using the observed [O III] $\lambda$ 4959 because [O III] $\lambda$ 4959 can have low S/N for galaxies with weaker emission lines (i.e. at higher masses). With dust-corrected  $R$  values, I determined electron temperatures following Nicholls et al. (2013):

$$T_e = a(-\log_{10}(R) - b)^{-c}, \quad (3)$$

where  $a = 13205$  K,  $b = 0.92506$ , and  $c = 0.98062$  (Nicholls et al. 2014). Figure 7 illustrates how  $R$  changes with  $T_e$  for composite measurements of the set of stacked spectra.

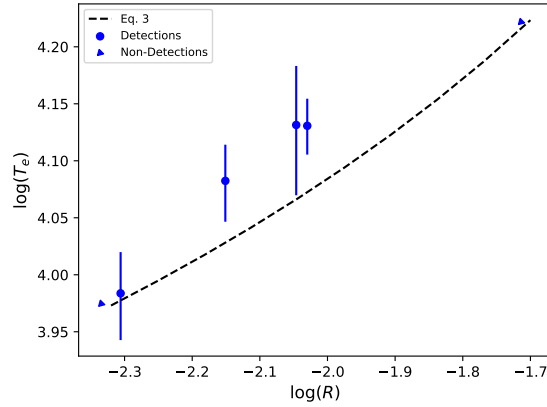


Figure 7: Dust-corrected  $\log(T_e)$  vs  $\log(R)$ . Composite spectra with detectable [O III] $\lambda$ 4363 are indicated with blue circles, and those with robust upper limits in  $T_e$  are represented by blue triangles.

I then used the computed electron temperatures to derive abundances for the two prominent species of oxygen atoms, O $^+$  and O $^{++}$ , with the following relations from Izotov et al. (2006):

$$12 + \log\left(\frac{\text{O}^+}{\text{H}}\right) = \log\left(\frac{[\text{O II}]}{\text{H}\beta}\right) + 5.961 \quad (4)$$

$$+ \frac{1.676}{t_2} - 0.4 \log(t_2)$$

$$- 0.034t_2 + \log(1 + 1.35x)$$

$$12 + \log\left(\frac{\text{O}^{++}}{\text{H}}\right) = \log\left(\frac{[\text{O III}]}{\text{H}\beta}\right) + 6.200 \quad (5)$$

$$+ \frac{1.251}{t_3} - 0.55 \log(t_3) - 0.014t_3.$$

Here, I utilized the [O II]/H $\beta$  and [O III]/H $\beta$  flux ratios and the following definitions:

$$t_3 \equiv 10^{-4} \cdot T_e, \quad (6)$$

$$t_2 \equiv 0.7 \cdot t_3 + 0.17, \text{ and} \quad (7)$$

$$x \equiv 10^{-4} \cdot n_e \cdot t_2^{-0.5}, \quad (8)$$

Table 4: Summary of Average Emission-line Flux Ratios and Derived Properties

Bin ID	Detection	$R$	$[\text{O II}]/\text{H}\beta$	$[\text{O III}]/\text{H}\beta$	$T_e$ [K]	$12 + \log(\text{O}/\text{H})$	$\log(\text{O}^+/\text{H})$	$\log(\text{O}^{++}/\text{H})$
(1)	(2)	(3)	(4)	(5)	(6)	(7)	(8)	(9)
1	D	$0.009^{+0.001}_{-0.001}$	$1.900^{+0.016}_{-0.015}$	$4.265^{+0.030}_{-0.030}$	$13511^{+760}_{-763}$	$8.129^{+0.083}_{-0.072}$	$-4.042^{+0.089}_{-0.078}$	$-4.360^{+0.071}_{-0.066}$
2	D	$0.009^{+0.003}_{-0.003}$	$2.489^{+0.023}_{-0.025}$	$4.352^{+0.038}_{-0.034}$	$13534^{+1714}_{-1792}$	$8.232^{+0.203}_{-0.164}$	$-3.897^{+0.211}_{-0.172}$	$-4.357^{+0.179}_{-0.134}$
3	D	$0.005^{+0.001}_{-0.001}$	$2.340^{+0.025}_{-0.025}$	$4.446^{+0.049}_{-0.041}$	$9632^{+836}_{-868}$	$8.577^{+0.164}_{-0.137}$	$-3.623^{+0.171}_{-0.143}$	$-3.858^{+0.153}_{-0.120}$
4	R	<0.005	2.601	3.598	<9432	>8.612	>-3.541	>-3.917
5	D	$0.007^{+0.001}_{-0.001}$	$2.753^{+0.022}_{-0.021}$	$3.298^{+0.024}_{-0.024}$	$12089^{+916}_{-958}$	$8.386^{+0.125}_{-0.111}$	$-3.705^{+0.128}_{-0.115}$	$-4.337^{+0.109}_{-0.090}$
6	R	<0.019	2.579	2.405	<16664	>7.726	>-4.421	>-4.814

(1) Stellar mass bin ID. (2)  $[\text{O III}]\lambda 4363$  detection where D=“Detection” and R=“Reliable non-detection.” (3) Flux ratio of  $\text{O}^{++}$  emission lines (see Eq. 2). (4) Flux ratio of  $[\text{O II}]\lambda 3727$  to  $\text{H}\beta$ . (5) Flux ratio of  $[\text{O III}]\lambda\lambda 4959, 5007$  to  $\text{H}\beta$ . (6) Electron temperature. (7) Logarithm of total oxygen abundance. (8) Logarithm of  $\text{O}^+/\text{H}$  abundance. (9) Logarithm of  $\text{O}^{++}/\text{H}$  abundance. For reliable non-detections, lower or upper limits are indicated.

where  $n_e$  is the electron number density; I adopted  $n_e = 10^3 \text{ cm}^{-3}$ .

These two ionic abundances were then combined to find the total oxygen metallicity in the gas:

$$\frac{\text{O}}{\text{H}} = \frac{\text{O}^+}{\text{H}} + \frac{\text{O}^{++}}{\text{H}}. \quad (9)$$

The electron temperature and metallicities are provided in Table 4. Following the error propagation explained in Section 3.4, metallicity uncertainties did not exceed approximately  $\pm 0.2$  dex.

## 5 RESULTS

With robust, derived metallicities for four of the seven stellar mass composites, I constructed a  $M_\star$ - $Z$  relation for high-redshift galaxies (see Figure 8). This relation describes how the metal content in galaxies depends on stellar mass. With comparison at different redshifts, it is possible to understand how galaxies have evolved.

To describe the shape of the  $M_\star$ - $Z$  relation, I fitted it with a curve in Figure 8. Here, I used the same functional form used in Andrews & Martini (2013), which was defined by Moustakas et al. (2011):

$$12 + \log\left(\frac{\text{O}}{\text{H}}\right) = 12 + \log\left(\frac{\text{O}}{\text{H}}\right)_{\text{asm}} - \log\left[1 + \left(\frac{M_{\text{TO}}}{M_\star}\right)^\gamma\right], \quad (10)$$

where  $12 + \log(\text{O}/\text{H})_{\text{asm}}$  is the asymptotic metallicity, or the limiting metallicity for high-mass galaxies;  $M_{\text{TO}}$  is the turnover mass, or the mass value where the curve begins to trend toward the asymptotic metallicity; and  $\gamma$  is the slope at the

low-mass end. I used the Python `scipy` library (`scipy.optimize.curve_fit`) with an initial guess of  $12 + \log(\text{O}/\text{H})_{\text{asm}} = 8.798$  and  $\gamma = 0.640$  (i.e., best-fitting values of Andrews & Martini 2013) as a baseline to fit the data points. Additionally, due to the small number (four) of composite spectra with  $[\text{O III}]\lambda 4363$  detection and three varying parameters in Eq. 10, I fixed the value of  $\log(M_{\text{TO}}/M_\odot)$  to 8.901 to more accurately constrain  $12 + \log(\text{O}/\text{H})_{\text{asm}}$  and  $\gamma$ . My final fitting parameters are  $12 + \log(\text{O}/\text{H})_{\text{asm}} = 8.693$  dex and  $\gamma = 0.621$ .

Next, I compared my  $M_\star$ - $Z$  relation with the relation in Andrews & Martini (2013) to gain a greater understanding of how the metal content in galaxies has evolved. On average, the Andrews & Martini (2013) curve is found to be  $\approx 0.1$  dex higher in metallicity than my curve in Figure 8, which is evident by the difference in  $\log(\text{O}/\text{H})_{\text{asm}}$  of 0.105 dex. This difference suggests a systematic increase in metallicities over the past seven billion years; however, it should be noted that this difference is within the margin of error. Specifically, my measurement uncertainties are on the order of 0.1 dex.

## 6 CONCLUSIONS

Characterizing gas properties of galaxies, such as electron temperature and gas-phase metallicity, gives insights for understanding galaxy evolution. However, the properties of high-redshift ( $z \approx 1$ ) galaxies are relatively poorly understood since less reliable methods and techniques have been used. The  $T_e$  method provides robust measurements of gas metallicity using the  $[\text{O III}]\lambda 4363$  emission line. However,  $[\text{O III}]\lambda 4363$  is a relatively weak emission line, so the signal from an individual galaxy is nearly un-

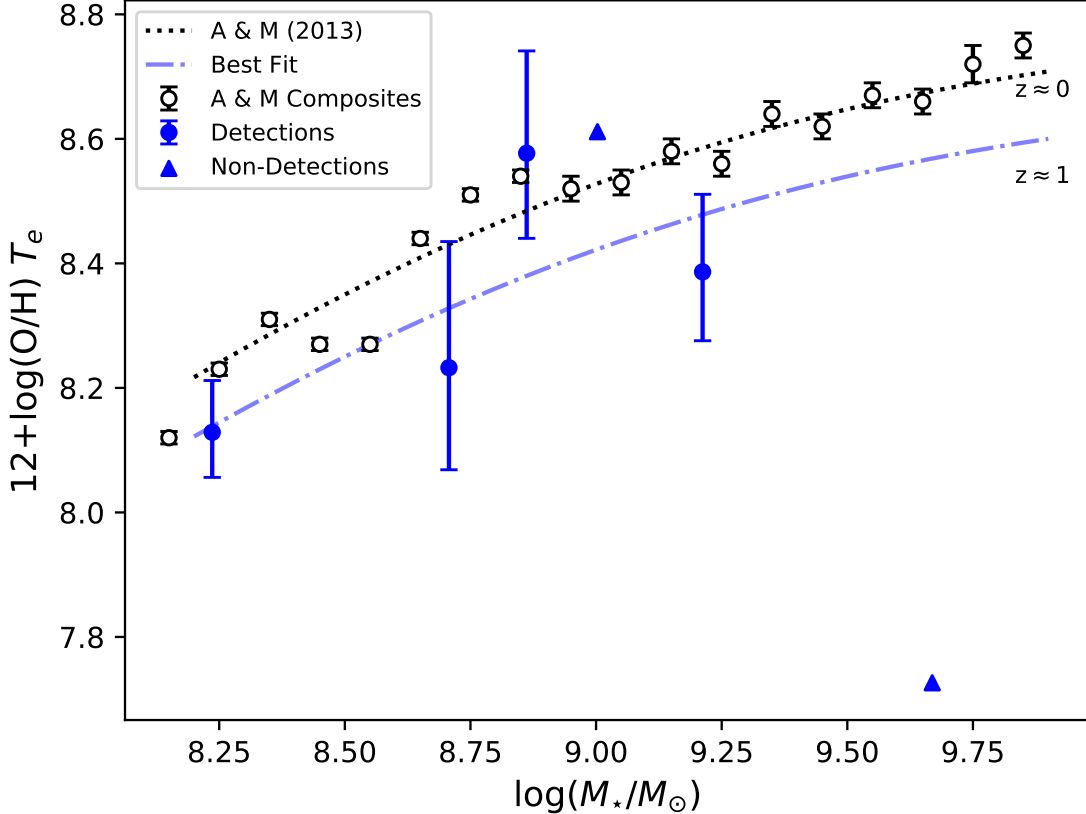


Figure 8: Dust-corrected  $M_*$ - $Z$  relation derived from stellar mass binned composite spectra. Overlaid is the  $M_*$ - $Z$  relation (black, dotted line) for local galaxies (Andrews & Martini 2013). My best fit is illustrated with the blue, dash-dotted line; blue circles (triangles) indicate composite spectra with detections (reliable non-detections) of  $[\text{O III}]\lambda 4363$ .

detectable. To account for this, several hundred spectra must be combined to enhance the signal of  $[\text{O III}]\lambda 4363$  to a detectable level.

One approach for selecting spectra to stack is to use a common property among the galaxies. Since the gas-phase metallicity is known to be tightly correlated with the stellar mass (Tremonti et al. 2004), constructing composite spectra for different stellar mass bins will yield a stellar mass-metallicity relation. In this project, I utilized  $\sim 4,000$  galaxy spectra at  $z \sim 1$  from the DEEP2 Galaxy Redshift Survey. I implemented a spectral stacking technique where I experimented with various stellar mass bin sizes to maximize the number of  $[\text{O III}]\lambda 4363$  detections while compensating for the varying strength of  $[\text{O III}]\lambda 4363$  with stellar mass (i.e.  $[\text{O III}]\lambda 4363$  is generally stronger with lower-mass galaxies). I found that seven stellar mass bins of varying size ( $N = 75 - 1443$ ) produced the most (four) detections of  $[\text{O III}]\lambda 4363$  while accurately accounting for its dependence on stellar mass. Using these stacked spec-

tra, I fit several emission lines to measure fluxes. Flux ratios between various emission lines were then used to derive dust attenuation corrections,  $T_e$ , and metallicities for each composite spectrum.

With a constructed  $M_*$ - $Z$  relation for  $z \approx 1$  galaxies, I fitted the relation following a functional form of Moustakas et al. (2011), and yielded a best fit of  $12 + \log(\text{O}/\text{H})_{\text{asm}} = 8.693$  dex and  $\gamma = 0.621$  with an assumed  $\log(M_{\text{TO}}/M_{\odot})$  of 8.901. Compared to local galaxies (Andrews & Martini 2013), my  $M_*$ - $Z$  relation is systematically lower ( $\approx 0.1$  dex) at a given stellar mass, which suggests a small increase in metals over the past seven gigayears.

## ACKNOWLEDGEMENTS

This research project was made possible through the use of data from the W. M. Keck Observatory, which is operated as a scientific partnership among the California Institute of Technology, the University of California and the National Aeronautics and Space Ad-

ministration (NASA). The Observatory was made possible by the generous financial support of the W. M. Keck Foundation. The author wishes to recognize and acknowledge the very significant cultural role and reverence that the summit of Maunakea has always had within the indigenous Hawaiian community. We are most fortunate to have the opportunity to conduct observations from this mountain. Additionally, funding for the DEEP2 Galaxy Redshift Survey was provided by several grants from the National Science Foundation and NASA.

I thank my project advisor, Dr. Chun Ly, for his support and direction throughout this entire project and the Arizona/NASA Space Grant Consortium for their professional development program and financial support during the 2019-2020 academic year. I am also grateful to the generous donors and members of the Galileo Circle who supported me financially throughout this project in 2019 and 2020.

## REFERENCES

- Aller, L. H. 1984, *Astrophysics and Space Science Library*
- Andrews, B. H. & Martini, P. 2013, *ApJ*, 765, 140
- Boquien, M., Burgarella, D., Roehlly, Y., et al. 2019, *A&A*, 622, A103
- Bruzual, G. & Charlot, S. 2003, *MNRAS*, 344, 1000
- Calzetti, D., Armus, L., Bohlin, R. C., et al. 2000, *ApJ*, 533, 682
- Cardelli, J. A., Clayton, G. C., & Mathis, J. S. 1989, *ApJ*, 345, 245
- Chabrier, G. 2003, *PASP*, 115, 763
- Faber, S. M., Phillips, A. C., Kibrick, R. I., et al. 2003, *Instrument Design and Performance for Optical/infrared Ground-based Telescopes*, 1657
- Izotov, Y. I., Stasińska, G., Meynet, G., et al. 2006, *A&A*, 448, 955
- Kewley, L. J., Dopita, M. A., Leitherer, C., et al. 2013, *ApJ*, 774, 100
- Leimbach, Reagen. (2020). *Recalibrating Strong-line Metallicity Diagnostics with Electron Temperature Measurements from Composite Spectra of Star-Forming Galaxies* (Bachelor's thesis, University of Arizona, Tucson, USA). <http://hdl.handle.net/10150/651369>
- Ly, C., Rigby, J. R., Cooper, M., et al. 2015, *ApJ*, 805, 45
- Matthews, D. J., Newman, J. A., Coil, A. L., et al. 2013, *ApJS*, 204, 21
- Moustakas, J., Zaritsky, D., Brown, M., et al. 2011, *arXiv:1112.3300*
- Newman, J. A., Cooper, M. C., Davis, M., et al. 2013, *ApJS*, 208, 5
- Nicholls, D. C., Dopita, M. A., Sutherland, R. S., et al. 2013, *ApJS*, 207, 21
- Nicholls, D. C., Dopita, M. A., Sutherland, R. S., et al. 2014, *ApJ*, 790, 75
- Osterbrock, D. E. 1989, *Astrophysics of Gaseous Nebulae and Active Galactic Nuclei*, by Donald E. Osterbrock. Published by University Science Books, ISBN 0-935702-22-9, 408pp, 1989.
- Storey, P. J. & Zeippen, C. J. 2000, *MNRAS*, 312, 813
- Tremonti, C. A., Heckman, T. M., Kauffmann, G., et al. 2004, *ApJ*, 613, 898